Nano Energy 135 (2025) 110659

Contents lists available at ScienceDirect

Nano Energy

journal homepage: www.elsevier.com/locate/nanoen

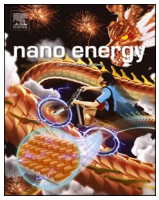

Full paper

A skin-inspired optoelectromechanically coupled system for 3-axis airflow sensor

Xiaozhong Wu [a], Ziyu Zhang [b], Haonan Zhao [a], Yang Wang [b], Junjie Zhou [a], Deyu Meng [a], Yanle He [a], Min Liu [a], Yifei Zhang [a], Zhongying Xue [c], Chengming Jiang [d,*], Miao Zhang [c], Zengfeng Di [c,*], Yongfeng Mei [b,*], Qinglei Guo [a,c,**]

[a] School of Integrated Circuits, Shandong University, Jinan 250100, PR China
[b] Department of Materials Science, International Institute for Intelligent Nanorobots and Nanosystems, Fudan University, Shanghai 200438, PR China
[c] State Key Laboratory of Materials for Integrated Circuits, Shanghai Institute of Microsystem and Information Technology, Chinese Academy of Sciences, Shanghai 200050, PR China
[d] State Key Laboratory of High-Performance Precision Manufacturing, Dalian University of Technology, Dalian 116024, PR China

ARTICLE INFO

Keywords:
Silicon nanomembrane
Airflow sensor
Skin-inspired electronics
Photodetectors
Optoelectromechanically coupled systems

ABSTRACT

Flexible airflow sensors that can detect the non-contact forces have broad prospects in environmental/climate monitoring, aircraft control, breathing monitoring, and human-computer interaction. Promising results have been achieved in terms of the sensing performances, however more challenging characteristics, such as the tunable detection range of airflow speed and 3-axis detection, are rarely investigated. Here, we demonstrate a skin-inspired optoelectromechanically coupled system, consisting of mechanically deformable elastic pillar array and photodetectors, for 3-axis airflow sensor. The mechanical deformation of elastic pillars induced by airflow can be optoelectrically coupled to photodetectors. As a result, variations in the collected photocurrent provide capabilities to quantitatively determine the speed of the incident airflow. Manipulating the Young's modulus and filling factor of elastic pillar array leads to tunable effective detection range of airflow speed. Through the integration of the developed optoelectromechanically coupled system on a hemispherical substrate, as well as the deep neural network processing, 3-axis airflow sensing is demonstrated. Our study may open an avenue to develop the high-performance airflow sensor, which can be further extended to various types of optoelectrically-based multifunctional sensors or systems by integrating other functional materials.

1. Introduction

The emergence of flexible biomimetic sensors that can mimic real body parts in appearance or functionality has promoted the development of health monitoring, human-computer interaction, robotics, and artificial intelligence [1–4]. With the advantages including mechanical flexibility, light weight, and compliance to non-planar surface, flexible biomimetic sensors can comfortably or imperceptibly integrate with objects to accurately detect physical signals or external stimuli [5–8], thus serving as functional platforms for the monitoring of physiological status (e.g., for human beings) or the operation status (e.g., for robots or aircrafts). In general, such sensors can measure a variety of physical parameters, such as temperature [9,10], pressure [11–13], humidity [14,15], and light intensity [16,17], in which the specific functionality is determined by the materials, device architectures, and sensing principles. In these cases, airflow sensation, which represents one of the most important human perceptions, is crucial for avoiding potential hazards induced by severe convection, informing appropriate wearing for health, predicting climatic variations, and other related. Compared to other rapidly progressed sensors, however, investigations on flexible biomimetic airflow sensor are far laying behind.

Nevertheless, various types of flexible biomimetic airflow sensors have been developed. The corresponding working principle includes airflow-induced temperature variations [18,19] or mechanical deformations [20,21], which can be further extracted by resistive/piezoresistive [22,23], piezoelectric [24], triboelectric [25,26], or magnetoelectric measurements [27]. Promising results have been demonstrated by these strategies, although current studies mainly focus

* Corresponding authors.
** Corresponding author at: School of Integrated Circuits, Shandong University, Jinan 250100, PR China.
E-mail addresses: jiangcm@dlut.edu.cn (C. Jiang), zfdi@mail.sim.ac.cn (Z. Di), yfm@fudan.edu.cn (Y. Mei), qlguo@sdu.edu.cn (Q. Guo).

https://doi.org/10.1016/j.nanoen.2025.110659
Received 11 November 2024; Received in revised form 22 December 2024; Accepted 7 January 2025
Available online 8 January 2025
2211-2855/© 2025 Elsevier Ltd. All rights are reserved, including those for text and data mining, AI training, and similar technologies.

on enhancing/improving one or two indexes associated with the device performance, including responsivity, response time, detection limit, and stability. More challenging characteristics, such as tunable detection range, 3-axis detection, and convenient fabrications, have been rarely evaluated. For instance, airflow sensors fabricated with nanomaterials exhibit good sensitivity and low detection limit [23,28], however, the detection range may be limited in return, possibly due to the insufficient mechanical strength of utilized nanomaterials. Meanwhile, the elastomer material has good mechanical properties to adapt to the wider sensing range, but the sensitivity needs to be further improved [20]. In addition to the airflow speed, the ability of 3-axis airflow sensing could help to construct more detailed information of the airflow field, which is required by many potential applications, such as climate monitoring [23], obstacle avoidance of aircrafts [18], and environment perception of robots [20]. At present, existing works that use airflow sensor arrays can successfully recognize the airflow direction in a two-dimensional plane [19,23,25], yet the 3-axis airflow sensing is challenged. Besides, convenient fabrication that compatible with the state-of-the-art semiconductor technology is also crucial for the production and development of flexible biomimetic airflow sensors.

In nature, insects use fine hairs all over their bodies to perceive the approaching predators or potential hazards [27,29]. Human skin covered with hair follicles can also sense the airflow to perceive the external environment [20,28]. Inspired by this, we herein demonstrate an optoelectromechanically coupled system, combining elastic polydimethylsiloxane (PDMS) pillars and silicon-based photodetectors, for flexible biomimetic airflow sensor. Similar to the skin hairs, the upper layer of PDMS pillars, which are dyed with carbon black [30,31], will deform by the non-contact force of airflow. As a result, changes in the projected light on the underneath photodetectors can be collected to quantify the airflow. In addition to high sensitivity, fast response time, and good stability, advantages of the demonstrated airflow sensor are

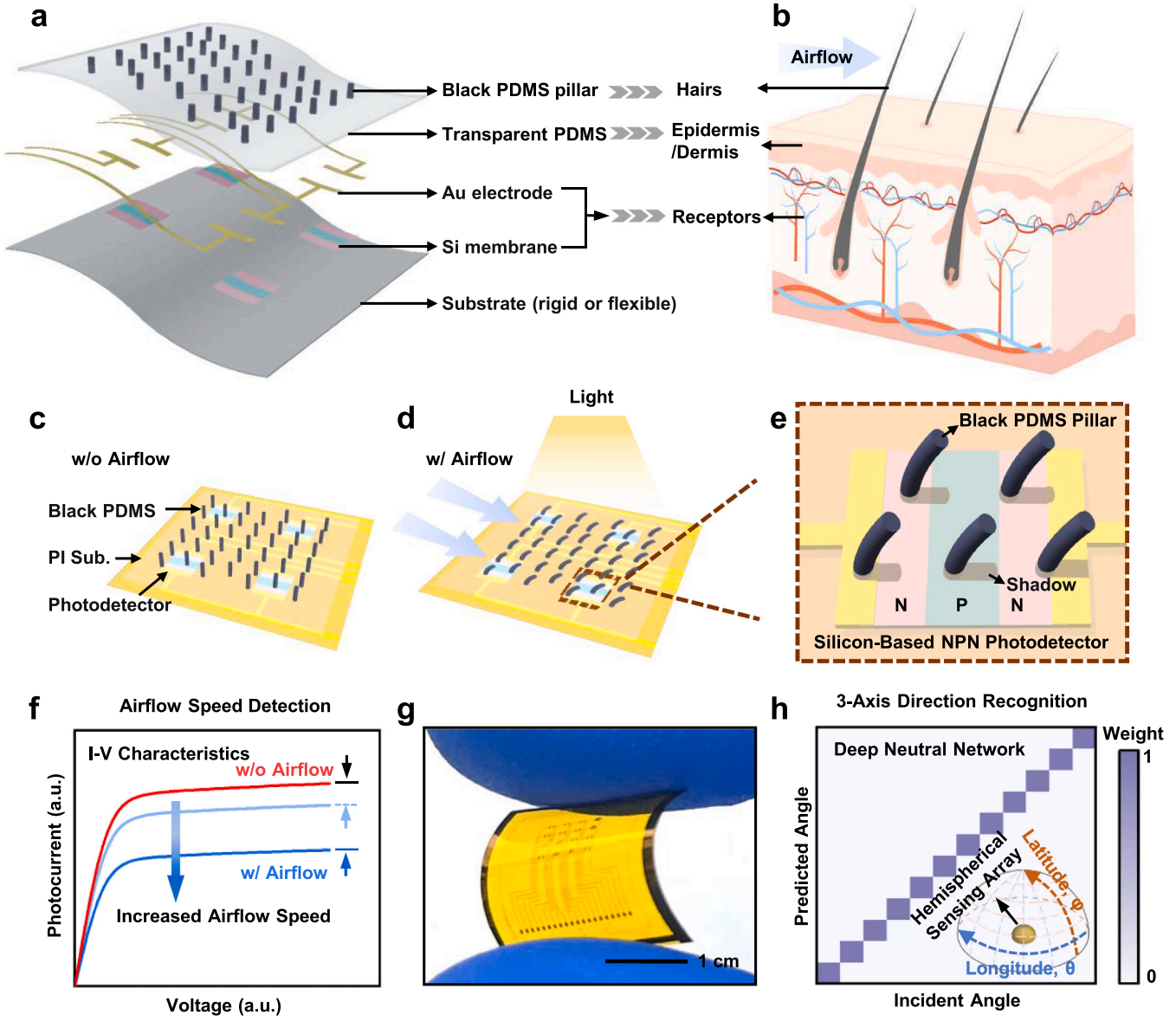

Fig. 1. Key materials and working principle of the optoelectromechanical airflow sensor. (a) Exploded Schematic of key materials and architectures. (b) Schematic diagram of the human skin with hairs, epidermis/dermis, and receptors. Schematics of an airflow sensor array without (c) and with (d) airflow. (e) A magnified diagram of the airflow sensor with airflow, which blows black PDMS pillars to deform. (f) Conceptual variations of photocurrents without (red curve) and with (blue curves) airflow. (g) Optical image of silicon-based photodetector array on flexible substrate. (h) Conceptual 3-axis direction recognition by a hemispherical sensing array through the deep neutral network. The inset shows the configuration for 3-axis airflow sensing, including the inner hemispherical sensing array, an outer shell for the airflow control, and the 3-axis direction referred to the latitude, φ and the longitude, θ.

also reflected in tunable effective detection range of airflow speed, and the capability of 3-axis airflow detection. Besides, the utilized materials and fabrications are compatible with the semiconductor technology, thus offering opportunities for the convenient design and mass production of the proposed airflow sensors.

2. Results and Discussion

2.1. Materials and working principles of the optoelectromechanical system

The schematic in Fig. 1a illustrates key materials and structures of the proposed optoelectromechanical airflow sensor, which consists of black PDMS pillar array, transparent PDMS layer, silicon-based photodetector, and the substrate from the top to the bottom. The whole configuration is inspired from the human skin, as shown in Fig. 1b, in which the top black PDMS pillars (dyed with carbon black) mimic the skin hairs that deform with airflow, and the underneath silicon-based photodetectors act as the receptors that optoelectrically collect airflow signals reflected by the deformation of the PDMS pillars. Fig. 1c schematically shows the airflow sensor in the static state, and the elastic black PDMS is vertical to the substrate. With the introduction of airflow, the elastic black PDMS will deform, accompanying with the direction and intensity of the airflow, as displayed in Fig. 1d. As a result, the illuminated light on the photodetector varies due to the formation of projected shadows, as shown in Fig. 1e, leading to changes in the photocurrent collected by the photodetector. Notably, the airflow speed can be quantified through the difference in photocurrents obtained without and with airflows, as revealed in Fig. 1f.

The ability to directionally recognize the airflow represents another advanced characteristic of the sensor. For the case of in-plane direction sensing, due to the attenuation of the airflow, black PDMS pillar near the airflow source deforms in a much larger degree than that far away from the airflow source, as demonstrated by the simulated results in Fig. S1a. Therefore, the airflow direction can be identified by the difference in response of sensors array (Fig. S1b). Moreover, the silicon-based

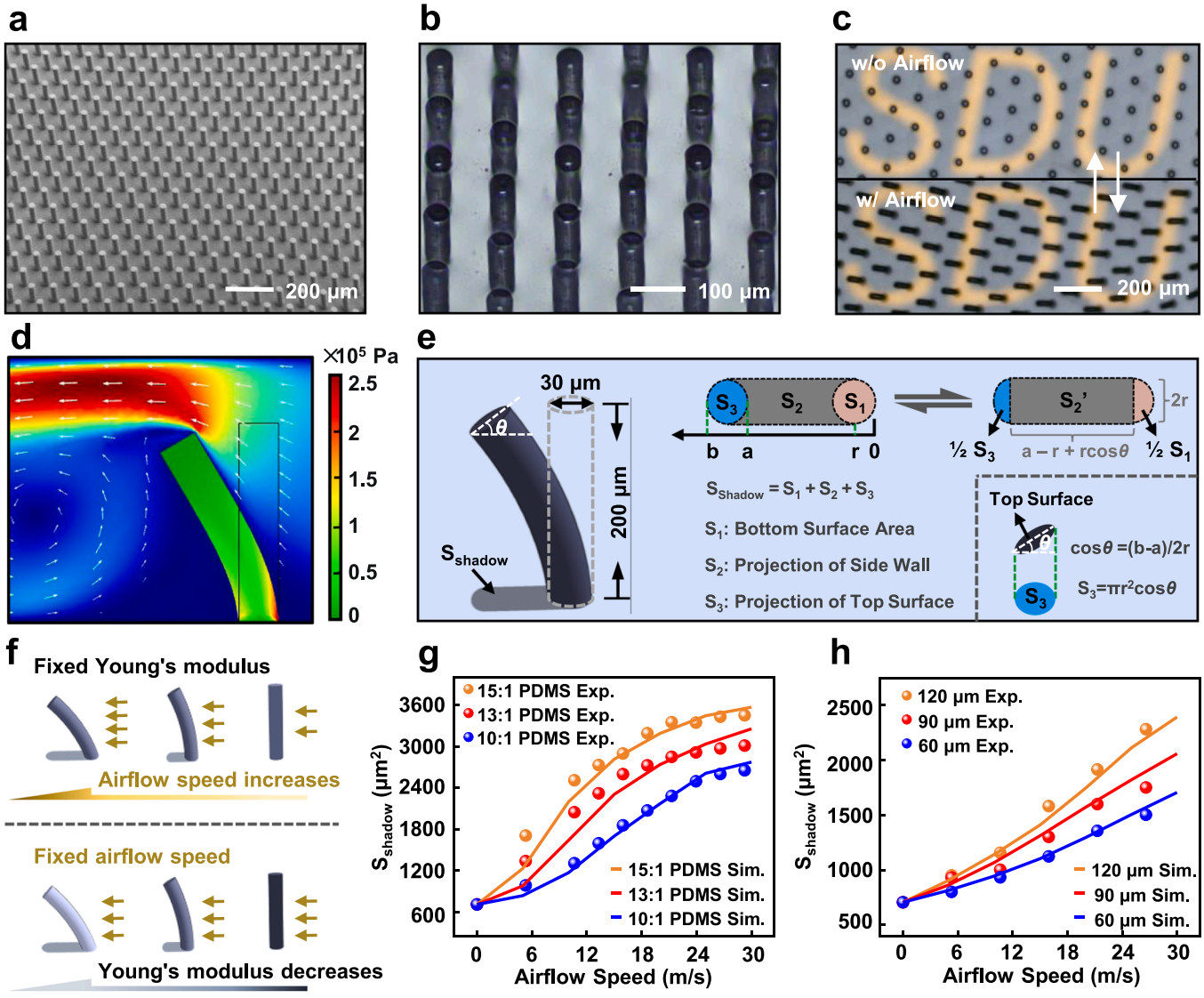

Fig. 2. Characterizations on black PDMS pillars/PDMS. (a) SEM image. (b) Optical microscope image. (c) Optical microscope images of the black PDMS pillar array on silicon substrate with patterned Au letters of "SDU", without (top) and with (bottom) airflow. (d) Simulated results of a bent black PDMS pillar induced by the airflow with a speed of 10 m/s. (e) Schematic of a bent black PDMS pillar and the methodology for calculating the projected shadow area. (f) Schematical deformations of elastic PDMS pillars under different airflow speeds (top, with fixed Young's modulus) and different Young's moduli (bottom, with fixed airflow speed). Simulated and experimental results of the projected shadow area varying with the airflow speed: (g) weight ratios of base to crosslinker for the preparation of black PDMS pillars are 15:1, 13:1, and 10:1; (h) neighboring distances of black PDMS pillar arrays are 120 μm, 90 μm, and 60 μm.

photodetector can be transferred to the flexible polyimide (PI) substrate by the transfer printing technique [32–36], as shown in Fig. 1g, with good flexibility. Meanwhile, the utilized viscoelastic PDMS also has good flexibility (Fig. S2). The combination forms flexible airflow sensor (or array, Fig. S3), which can be further amounted on other substrates with complex surfaces, for example, a hemispherical substrate. As a result, 3-axis airflow detection is realized through the deep neural network analyses of the photocurrents collected from the hemispherical sensor array, as schematically shown in Fig. 1h.

In the proposed optoelectromechanical airflow sensor, the black PDMS pillar layer plays an essential role for airflow sensing. Fig. S4 schematically shows the corresponding preparation process. A patterned epoxy-based photoresist (SU-8, Micro Chem.) layer is used as the mold to obtain black PDMS pillar array. Details about geometry and arrangement of the SU-8 mold can be found in Fig. S5. Notably, the pillar array configuration is designed as hexagonal, which has a much larger integrated density compared to that of the tetragonal arrangement. The mixture of PDMS and carbon black is drop-casted onto the SU-8 mold. Shaving-off the excess black PDMS on the surface leaves them only existing within the mold. Then, another PDMS layer (without carbon black) is spin-coated. After fully cured on a hot plate, black PDMS pillar array vertically stacking on a transparent PDMS layer can be peeled-off, as shown in Fig. 2a (scanning electron microscope, SEM) and Fig. 2b (optical microscope image). Notably, the black PDMS pillars can deform with the airflow to alter the illuminated light on the underneath photodetectors, and transparent PDMS layer allows for the light transmission.

The top panel of Fig. 2c shows the optical microscope image of a black PDMS pillar/PDMS, covering on a substrate with the abbreviations "SDU" of Shandong University. At the static state (i.e., without airflow), good transparency of PDMS enables the clear seeing of SDU. After the introduction of airflow, the abbreviation becomes obscure due to the deformation of black PDMS pillars, as shown in the bottom panel of Fig. 2c. Due to the good elasticity of PDMS, the clear or obscure seeing of SDU is reversible. Fig. S6 provides more optical microscope images of the black PDMS pillars at different deformation states in either cross-section or planar views. As the increase of the airflow speed, black PDMS pillars deform more acutely. Fig. 2d presents the simulated result of a deformed PDMS pillar at an airflow speed of 10 m/s, which exhibits the similar deformation behavior with the experimental results (Fig. S6). Since the projected shadow induced by the deformation of black PDMS pillars strongly determine the variations in photocurrent, calculating the shadow area is crucial for quantifying the airflow speed. Herein, the selected PDMS pillars that are used for the shadow calculation have a certain distance away from the airflow source (herein, 900 μm). Fig. 2e illustrates a typical deformed black PDMS pillar, as well as the model for calculating the projected shadow area (S_{shadow}) by a light irradiation from the vertical direction (see the derivation process in the Experimental Section). As a result, S_{shadow} can be expressed as,

$$S_{shadow} = \frac{1}{2}\pi r^2 - 2r^2 + \left(1 - \frac{\pi}{4}\right)ra + \left(1 + \frac{\pi}{4}\right)rb \quad (1)$$

where a is the distance of the projection of the pillar highest point to point "o", b is the distance of the projection of the leftmost point to point "o", and r is the radius of the pillar. For the calculations of experimental and simulated S_{shadow}, the corresponding values of a and b can be directly measured from the deformed pillars captured by the optical microscope and simulations, respectively.

The mechanical property of elastic PDMS pillars could strongly determine their deformation behavior, which is crucial for the performance, such as sensitivity and detection range, of the proposed airflow sensor. With fixed Young's modulus, the deformation degree of PDMS pillar increases, until the saturation reaches, with the increase of the airflow speed, resulting in an enlarged projected shadow area, as schematically shown in the top panel of Fig. 2f. Once the speed of incident airflow is fixed, elastic PDMS pillar with large Young's modulus is too stiff to deform. Reducing the Young's modulus of the elastic PDMS pillar could gradually strengthen its deformation degree, i.e., the projected shadow area, as illustrated in the bottom panel of Fig. 2f. To verify these analyses, both experimental investigations and theoretical simulations are performed.

Fig. 2g shows both experimental and simulated results of the projected shadow area varying with the airflow speed. Three kinds of PDMS that the weight ratios of base to crosslinker are set as 10:1, 13:1, and 15:1, are utilized to create black pillars. For all types of black PDMS pillars, the experimental results agree well with the simulations, indicating the accurate and stable responses of black PDMS pillars to the airflow. Moreover, because the Young's modulus of PDMS is strongly related to the weight ratio of base to crosslinker [37], PDMS pillars with a much larger weight ratio deform more acutely compared to those with a much lower weight ratio, as revealed by the significant increase of the shadow area at the same airflow speed. Besides, the filling factor of PDMS pillars also influences their deformations. As demonstrated in Fig. 2h, PDMS pillars with a much larger distance between two neighboring pillars, corresponding to a much smaller filling factor, will deform more acutely compared to those with a much smaller neighboring distance, suggesting a much weaker interaction between the pillars. These presented results will provide guidelines for the design and fabrication of high-performance airflow sensors, which are determined by the synergistic effect between the Young's modulus and filling factor of black PDMS pillar array.

2.2. Optoelectronic characteristics of airflow sensors

For the proposed optoelectromechanical airflow sensor, the deformation of black PDMS pillars induced by airflow can be captured by the underneath photodetectors. In this regard, silicon-based photodetectors, with a typical NPN structure [38–40], are fabricated, as shown in Fig. 3a. Detailed fabrication process is schematically illustrated in Fig. S7. The following combination with black PDMS pillar/PDMS (Fig. 3b) forms the optoelectromechanical airflow sensor, as shown in Fig. 3c. Although the increase in the photodetector size allows for more numbers of PDMS pillars falling within the photodetection range, the ratio of shadow area and device size is unchanged under the same airflow condition. On the other hand, the increase of the photodetector size will cause uncertainty, such as cracks due to the excessive stress induced by the deformation of the elastic stamp [41,42], into the transfer printing of silicon nanomembranes. Current-voltage (I-V) characteristics of the silicon-based photodetector, prior to the combination with black PDMS pillar/PDMS, in Fig. 3d reveal good optoelectronic performances. A laser with a wavelength of 635 nm and tunable light power density is utilized as the light source. Fig. S8 summarizes the photocurrent obtained from the photodetector (biased at 1 V) varying with the illuminated light power density, exhibiting an obvious linear relationship. Moreover, after transferring the photodetector onto flexible PI substrate, the photocurrent presents negligible variation before and after 500 bending cycles (bending radius: about 0.8 cm), as shown in Fig. S9. The fabrication of flexible silicon-based photodetectors can be found in Fig. S10 and the Experimental Section.

Good and mechanically stable optoelectronic performances of the fabricated silicon-based photodetectors provide the basis for the airflow detection. Fig. 3e shows the I-V characteristics of the fabricated airflow sensor. Nitrogen airflow is introduced with the speed being controlled by a gas flowmeter (Fig. S11). The light power density is constant as 25.48 mw/mm^2 during the measurement. As the increase of the airflow speed, the obtained photocurrent decreases due to the increased shadow area projected onto the photodetector. According to the magnified results of I-V characteristics (see Fig. S12), the relationship between photocurrent (biased at 1 V) and airflow speed appears in Fig. 3f. For this specific airflow sensor, in which the weight ratio of base to crosslinker and the distance of two neighboring pillars are 10:1 and 120 μm,

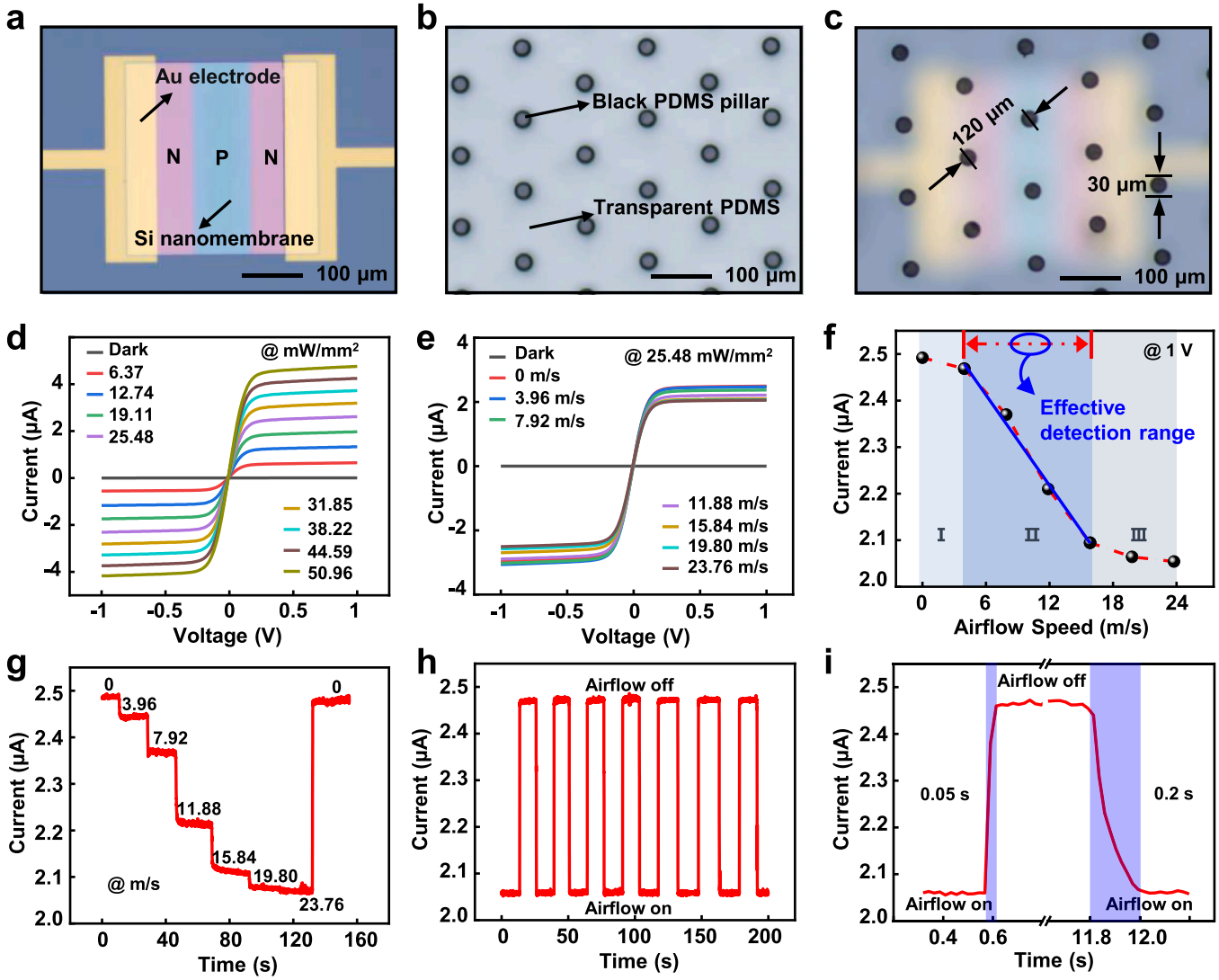

Fig. 3. Assembly and characteristics of optoelectromechanical airflow sensor. Optical microscope images of (a) a silicon-based NPN photodetector, (b) a black PDMS pillar array on transparent PDMS substrate, and (c) an optoelectromechanical airflow sensor. (d) I-V characteristics of the photodetector under different light power intensities (laser wavelength: 635 nm). (e) I-V characteristics of the airflow sensor under different airflow speeds. (f) Photocurrents extracted at 1 V varying with the airflow speed. (g) Real-time variations of photocurrent under the continuous introduction of airflow with different speeds. (h) Real-time variations of photocurrents under the introduction of a pulsed airflow with a speed of 15.84 m/s. (i) A magnified cycle of photocurrent variation, showing the response time of the sensor.

respectively, moderate decrease in the photocurrent within a low speed range (< 3.96 m/s, Region I) is observed, due to the intrinsic mechanical strength of PDMS pillars. At the relatively large speed range (>15.84 m/s, Region III), the deformation of the PDMS pillar approximates to be gradually saturated, thus leading to slight decrease in the photocurrent. Within the speed range of 3.96–15.84 m/s (Region II), the fabricated airflow sensor exhibits a high sensitivity of 1.3 %s/m. Herein, the airflow speed range in which a specific airflow sensor has the highest sensitivity is defined as the effective detection range, as displayed in Fig. 3f. Fig. 3g shows the real-time response of the sensor to airflows with different speeds. Once withdrawing the applied airflow, photocurrent can recover to its initial value, implying the good stability of the fabricated airflow sensor.

The long-term stable response of the sensor is further investigated by introducing a pulsed nitrogen airflow, and the airflow speed is 15.84 m/s. Fig. 3h shows the measured photocurrent from the sensor responding to the pulsed airflow, and steady photocurrent variations at either "airflow on" or "airflow off" states imply the long-term stability of the fabricated sensor. The response time of the sensor is extracted from one period of the pulsed airflow. As shown in Fig. 3i, the sensor takes about 0.2 s to effectively detect the introduction of airflow, and recovers to its initial state within 0.05 s. The much higher response time to the introduction of airflow, compared with that to the withdrawing of airflow, could be attributed to the time consuming by PDMS pillars to achieve a stable mechanical deformation. In addition, the developed airflow sensor also exhibits good responsivity and repeatability at low speed, as shown in Fig. S13.

According the working principle of the proposed airflow sensor, the deformation status of elastic PDMS pillars will govern the sensing performance, especially for the effective detection range of the airflow speed. As shown in the left panels of Fig. 4a, stiff PDMS pillar array will be straight without deformation, and soft PDMS pillar array easily reaches saturated deformation. These typical issues can be addressed by manipulating the Young's modulus and/or filling factor of PDMS pillars, as shown in the right panel of Fig. 4a. Fig. 4b presents the normalized photocurrent, obtained from five types of airflow sensors featured by weight ratio and neighboring distance of utilized PDMS pillars, varying with the airflow speed. The sensitivity and effective detection range (see the definition in Fig. 3f) of airflow sensors can be tuned by the control over the Young's modulus and filling factor of PDMS pillars. Notably,

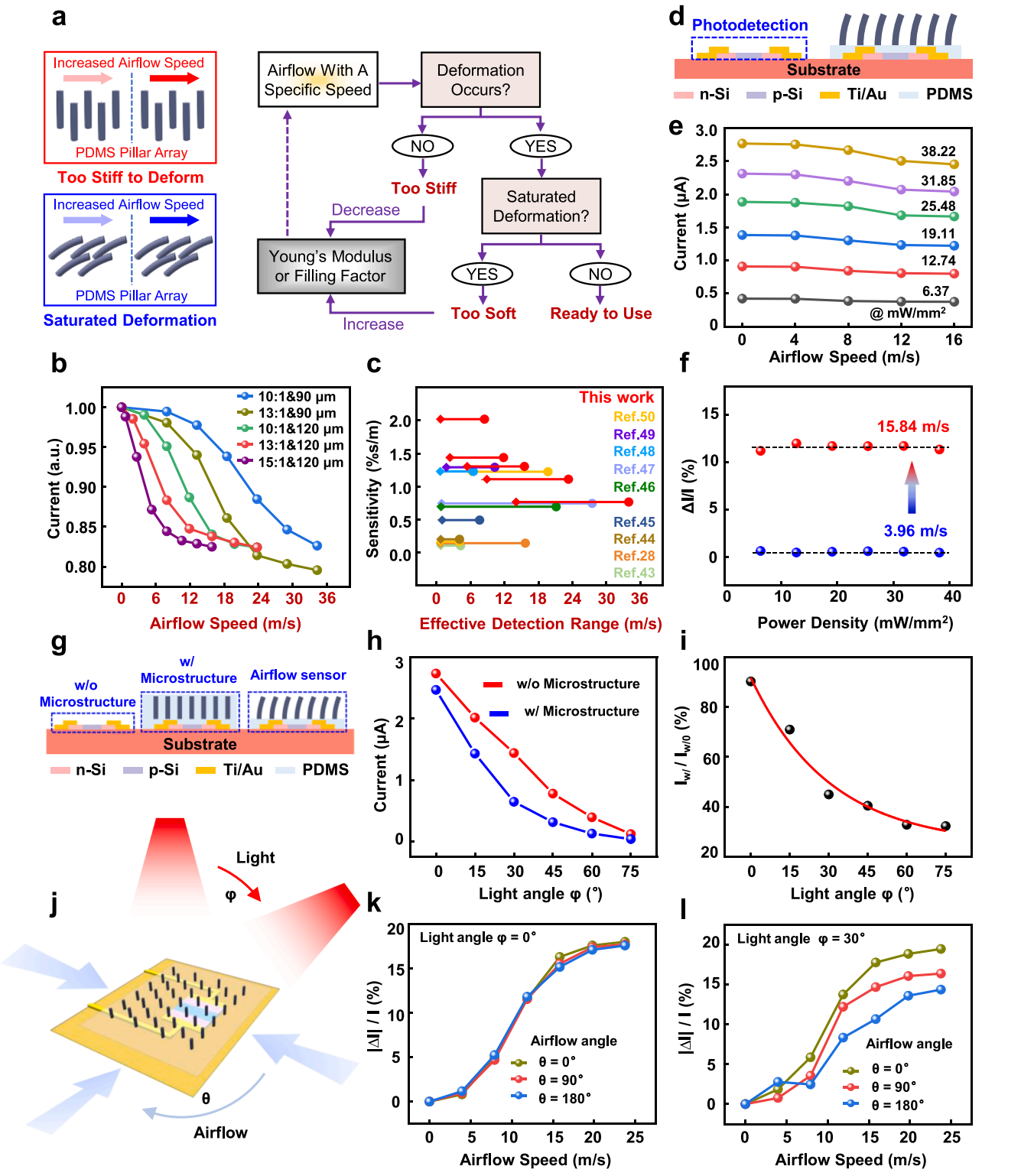

Fig. 4. Characterization and optimization of the airflow sensor. (a) Typical issues (left) and optimization flow chart (right) of the airflow sensor. (b) Photocurrent variations with the airflow speed obtained from different optoelectromechanical sensors, of which the black PDMS pillars have different weight ratios of base to crosslinker and neighboring distances (i.e., filling factors). (c) Comparisons in effective detection range and sensitivity of the demonstrated sensor with those of other previous reports [28,43–50]. (d) Schematic of the simultaneous operation of photodetection and airflow sensing. (e) Photocurrents obtained from the airflow sensor varying with the airflow speed under different light power intensities. (f) Changes in photocurrent varying with the light power density for two typical airflow speeds. The change in photocurrent exhibits negligible relationship with the incident light power density, but is strongly determined by the airflow speed. (g) Schematic of the simultaneous operation of light incident direction recognition and airflow sensing. (h) Photocurrents obtained from the photodetectors with and without microstructured layer varying with the light illumination angle φ. (i) The ratio of photocurrent obtained from the photodetectors with and without microstructured layer varying with the light illumination angle φ. (j) Schematic of airflow sensing under different illumination angles (φ) and airflow angles (θ). Airflow speed sensing under different airflow angles: (k) illumination angle φ= 0°; (l) illumination angle φ= 30°.

with the increase of the weight ratio or the neighboring distance, the sensitivity becomes much higher (evidenced in Fig. S14) though the effective detection range becomes shortened. This problem can be circumvented, to some extent, by the airflow sensor, which has varying Young's moduli or filling factors of the PDMS pillar array. As an example, airflow sensor that contains PDMS pillar arrays with different Young's moduli (the corresponding weight ratios of base to crosslinker are 15:1 and 10:1, respectively) exhibits a broad sensing range of airflow speed with high sensitivity, as demonstrated in Fig. S15. As a result, the demonstrated optoelectromechanical airflow sensor with tunable effective detection range of speed has a much higher sensitivity than those of previously reported works, as summarized in Fig. 4c. More details about the comparison of the airflow sensing performances with other works can be found in Table 1.

It should be noted that the light source is indispensable for the detection of airflow by the proposed optoelectromechanical sensor. For practical applications, airflow detection performances under different light irradiation conditions should be consistent. In this case, the photodetection component can be integrated with the airflow sensor to monitor the illuminated light intensities, as shown in Fig. 4d. Fig. 4e shows the photocurrent variations of the airflow sensor with the airflow speed under different light power intensities. For two different airflow conditions (e.g., airflow speeds are 3.96 m/s and 15.84 m/s), changes in photocurrent, which is defined as the ratio of the difference in photocurrents obtained with and without airflow to the initial photocurrent (without airflow), under different light irradiation intensities appear in Fig. 4f. It can be found that at a specific airflow speed, the light power intensity has little influence on the photocurrent change. In other words, the photocurrent change is merely depended on the airflow speed.

In addition, the light incident direction may also cause uncertainty to the optoelectronic response of the sensor. To explore the influence of light incident direction on the airflow sensing, device configuration shown in Fig. 4g is designed. The two sensors on the left are pure photodetector (labeled as, w/o Microstructure) and photodetector covered by a designed microstructured layer (labeled as, w/ Microstructure), respectively. Notably, the microstructured layer consists of a black PDMS pillar array embedded in a transparent PDMS. Therefore, airflow-induced deformation of the embedded black PDMS pillars can be avoided. As a result, the projected shadow area on the top surface of the photodetector (w/ Microstructure) is only determined by the light incident direction. Fig. 4h shows photocurrents measured from the sensors with and without microstructure under different illumination angles (φ), defined as the angle between the light incident direction and the vertical direction (see Fig. S16). It can be found that the current ratio $I_{w/}$ / $I_{w/o}$ is monotonously determined by φ, as shown in Fig. 4i. As a result, the light incident direction can be revealed. Fig. 4j schematically illustrates the airflow sensing under different illumination angles (φ) and airflow angles (θ). For the condition that the light illumination is perpendicular with the horizontal plane (i.e., φ=0°), airflow sensing at different airflow angles are almost consistent, as revealed in Fig. 4k. Otherwise, e.g., φ= 30°, photocurrent changes under different airflow angles exhibit similar trends though no longer coincident, as shown in Fig. 4l. Nevertheless, the photocurrent has a certain relationship with the airflow speed once determinations of the light incident direction (Fig. 4i) and airflow angle (see Fig. S17) are accomplished. Although the data acquisition and processing are relatively complicated and massive, utilizing the proposed device structure (Fig. 4g) can theoretically provide capabilities for the airflow sensing regardless of the ambient light condition. However, utilizing a simulated light that is perpendicular with the horizontal plane as the illumination source is recommended due to the simplicity of the data processing.

2.3. 3-axis airflow detection

Since the fabrication of the proposed airflow sensors, including black PDMS pillars and silicon-based photodetectors, is compatible with the state-of-the-art semiconductor technology, it is convenient to construct airflow sensor array for the directional detection. Figs. S17a-S17c schematically illustrate a 4 × 4 pixels sensor array under different airflow conditions. Due to the existence of airflow resistance and attenuation, changes in photocurrent obtained from the sensor array gradually decreases as the propagation of airflow, as shown in Figs. S17d-S17f, thus offering possibilities to identify the in-plane airflow direction. At the same time, the sensing pixel at the array edge that close to the airflow source can used to evaluate the airflow speed.

Although a planar sensor array can identify the in-plane airflow direction and speed, it may be unsuitable for the 3-axis airflow detection. Previous studies have demonstrated that the hemispherical array structure can realize the 3-axis detection of physical parameters, such as light and temperature [53–56]. Taking the advantage of transferrable silicon photodetectors onto flexible substrate, a hemispherical airflow sensor array consisting of 7 sensing units is fabricated, as shown in Fig. 5a. Among them, 6 sensing units in a circular array are used to identify the incident angle, and the seventh sensor at the top is utilized to identify the airflow speed. The light source is positioned right above the hemispherical sensing array. And the light incident direction is perpendicular with the horizontal plane. The illumination area covers the entire hemispherical array. Therefore, the shadow area projected on the photodetector surface is only determined by the induced airflow condition, i.e., airflow angle and speed. Details about the design and

Table 1
Comparisons on the key parameters of the demonstrated optoelectromechanical airflow sensor with those of previously reported works.

Ref.	Materials	Principle	Response time	Sensitivity	Detection range
[28]	Si wires	Piezoresistive	0.04 s	0.137 %s/m	0.15–15.3 m/s
[43]	PEDOT: PSS fibers		0.05 s	0.12 %s/m	to 3.5 m/s
[44]	CNTs/RGO film*		1.04 s	0.2 %s/m	0.0176–3.5 m/s
[45]	CNTs/CSF*		1.3 s	0.5 %s/m	0.05–7 m/s
[46]	SCNT-CNs*		0.0211 s	0.7 %s/m	0.02–21 m/s
[48]	SCNT-CNs*		0.021 s	1.24 %s/m	0.11–6 m/s
[49]	CNTs*		0.12 s	1.3 %s/m	1–10 m/s
[47]	Ni/W	Thermoresistive	–	0.75 %s/m	0.5–30 m/s
[50]	GaN	Optical	0.013 s	0.17 %s/m	0.1–5.84 m/s
				1.24 %s/m	5.84–21.29 m/s
[51]	Optical fiber		–	24.9 pm/(m/s)	20–36 m/s
[52]	Optical fiber		–	0.22 nm/(m^3/h)	1–6.5 m^3/h
This work	PDMS Pillar/Silicon	Optoelectro-mechanical	0.2 s/0.05 s	2.02 %s/m	0.66–7.92 m/s
				1.43 %s/m	1.98–11.88 m/s
				1.3 %s/m	3.96–15.84 m/s
				1.1 %s/m	7.92–23.76 m/s
				0.75 %s/m	13.2–34.32 m/s

* Full names of abbreviations are: SCNTNs-suspended ultralong carbon nanotube crossed networks; CNTs-carbon nanotubes; RGO-reduced graphene oxide; CSF-carbonized silk fabric.

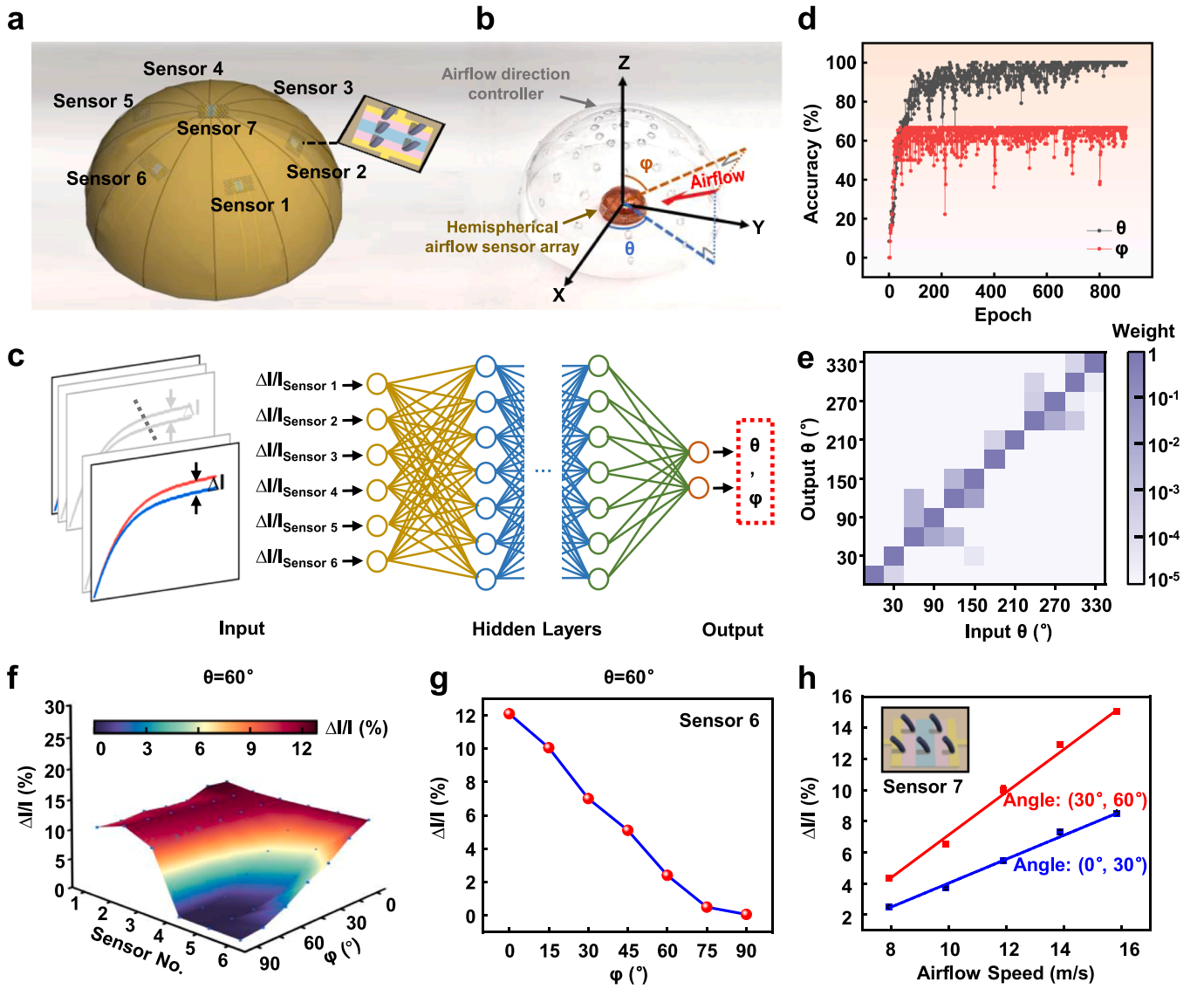

Fig. 5. 3-axis airflow recognition. (a) Schematic of a hemispherical airflow sensor array. (b) Optical image of the hemispherical airflow sensor array and the airflow direction controller. The three-dimensional coordinate is used to define the angle of the incident airflow, i.e., (θ, φ). (c) Schematic of deep neural network assisted analysis of the airflow angle. (d) The epoch-dependent recognition accuracy of training set in θ and φ using deep neural network. (e) Weight mapping of output θ with different values of input θ (φ=60°). (f) Photocurrent changes of the 6 sensing units under the incident airflow with varying φ and constant θ (60°). (g) Photocurrent changes of the sensor 6 under different values of φ (θ=60°). (h) Photocurrent changes of the sensor 7 varying with the airflow speed under two different airflows.

configuration of the hemispherical sensor array can be found in Fig. S18, Fig. S19, and the corresponding descriptions in the Experimental Section. To realize the airflow with different incident angles, a hemispherical omnidirectional airflow controller is designed. The controller consists of a transparent PMMA hemispherical housing and an array of holes in which the incident airflow can manipulated at a specific angle. The prepared hemispherical airflow sensor is placed right below the airflow controller, as shown in Fig. 5b. The incident angle (θ and φ in Fig. 5b) of the airflow is calibrated (Fig. S20). As an example, the angle of airflow, shooting from the red point in Fig. S20, is calibrated as θ= 60°, and φ= 60°, i.e., (60°, 60°).

Under different incident airflow angles, the 6 circular sensing units would have independent responses, reflecting in the corresponding photocurrent changes. Then, the collected photocurrent change data are imported into the neural network for incident angle analysis (Fig. 5c). Based on the different responses of the 6 circular sensing units, either to a specific airflow or to different airflow conditions, deep neural network algorithm can build an angle-sensitive detection model, which can be used to recognize the incident angle, (θ, φ). After that, a set of photocurrents data is collected as input for the training of deep neural network. As shown in Fig. 5d, the accuracy of the training set for recognizing the angles of θ and φ are 98 % and 67 %, respectively. At φ= 60°, the accuracy for recognizing θ is closed to 100 %, as shown in Fig. S21. The weight of correct prediction for θ, as shown in Fig. 5e, is more than 10 times compared to that of wrong prediction. Although the accuracy for recognizing φ is only 67 %, it can be further identified once θ has been recognized.

Fig. 5 f shows the photocurrent changes collected from the 6 sensing units under the incident airflow with varying φ and constant θ (60°). After extracting the response curve of each sensor (Fig. S22), it is found that the response curve of sensor 6 exhibits significant variations with φ, as shown in Fig. 5 g. In addition, under other values of θ (e.g., 180° and 300°), a specific sensor within the circular sensor array always exists for the identification of φ, as shown in Fig. S23. These presented results demonstrate strong supplementary with the deep neural network algorithm for the accurate recognition of φ, thus providing effective directional detection of the incident airflow. Apart from the spatial direction recognition, airflow speed detection is also essential for a real sense of 3-

axis airflow sensor. Once the spatial direction of the airflow is identified, the seventh sensor at the top of the hemispherical substrate could determine the airflow speed. For this purpose, the photocurrent changes of the seventh sensor varying with θ, φ, and airflow speed should be already measured, which is indeed a complicated and massive task. For the sake of simplicity, two spatial directions of the airflow are randomly selected. As shown in Fig. 5 h, the obtained photocurrent changes exhibit a good linearity with the airflow speed, conceptually demonstrating the capability of the proposed optoelectromechanically coupled system for 3-axis airflow sensing.

3. Conclusion

Inspired by the human skin, we herein report materials, device architectures, fabrications, and characterizations of an optoelectromechanical airflow sensor, which consists of a skin hair-like black PDMS pillar layer, a transparent PDMS membrane, and a silicon-based photodetector. The deformation of black PDMS pillars with the introduction of airflow can be optoelectrically coupled to silicon-based photodetectors. As a result, both the speed and the direction of the incident airflow can be detected or recognized. In addition to high sensitivity, fast response time, and good stability, key advantages of the proposed airflow sensor include: 1) the convenience for tuning the effective detection speed range of airflow by manipulating the Young's modulus and filling factor of black PDMS pillars; 2) the possibility of 3-axis airflow detection realized by a hemispherical sensor array; 3) the compatibility of the fabrication process with the semiconductor technology, which offers opportunities for the convenient design and mass production of the proposed airflow sensors. The proposed optoelectromechanical system can be extended by integrating other functional materials with high-performance photodetectors, which may lead to the development of various optoelectrically-based multifunctional sensors or integrated systems.

4. Experimental section

Fabrication of silicon-based photodetectors: The fabrication of silicon-based NPN photodetector began with a clean silicon-on-insulator (SOI) wafer (see Fig. S7), in which the thicknesses of top silicon (P-type, resistivity: 8.5–11.5 Ω.cm) and buried oxide layer are 120 nm and 2 μm, respectively. SiO_2 layer with a thickness of 600 nm was deposited by plasma enhanced chemical vapor deposition (PECVD) on the SOI wafer as the barrier for the following selective doping process. Then, phosphate-based spin-on-dopant (P509, Filmtronics) was coated and annealed at 1000 °C to complete the selective doping. After that, a 4 × 4 pixels array composed of 300 μm× 300 μm NPN photodetection structure is obtained by photolithography and dry etching. Finally, the deposition of 50 nm Au layer formed the electrodes of photodetectors. For the preparation of the flexible photodetector (Fig. S10), the transfer of silicon-based NPN photodetection structures on flexible PI substrate was realized by the photoresist-anchored transfer printing technique, which can be found in our previous work [32]. After that, the Au electrodes with a thickness of 50 nm were deposited to obtain flexible photodetectors.

Fabrication of black PDMS pillar/PDMS: The fabrication process can be found in Fig. S4. Firstly, SU-8 photoresist was used to make a microporous mold, with a hexagonal layout of opening cylinders (diameter: 30 μm, height: 200 μm, Fig. S5) on silicon substrate. Then, the PDMS mixture (Sylgard 184, DOW Corning) and carbon black (particle size: 25 nm, Orion Printex) were thoroughly mixed (weight ratio of crosslinker to carbon black: 10:1) to obtain the black PDMS mixture, which was drop-casted to the SU-8 mold. After shaving-off the excess black PDMS on the surface, PDMS mixture with a weight ratio of base to crosslinker of 10:1 was spin-coated the surface. After fully curing by the annealing treatment at 80 °C on the hot plate, the black PDMS pillar/PDMS could be obtained.

Fabrication of airflow sensors: Prior to integrating the obtained black PDMS pillar/PDMS with silicon-based photodetectors, an ultra-thin PDMS layer was spin-coated onto the silicon-based photodetectors. Then, the black PDMS pillar/PDMS was attached to the photodetector. The following curing of the ultra-thin PDMS layer by the annealing treatment at 80 °C on the hot plate induced a tight interface, which can sustain the airflow with a high speed without delamination.

Characterizations: Nitrogen cylinder was utilized as the airflow source, of which the release speed could be adjusted by a throttle valve, and airflow speed was quantified via a gas flow meter (Fig. S11, MF 5706, Siargo Ltd.). For the introduction of pulsed airflow, a custom-made cover was used to circularly shield the airflow. The optoelectronic characterizations were carried out by a custom-made photoelectric test platform, in which a 635 nm laser (MRL-III-635, CNI Laser) was used as the light source, with the light power density being measured via a light power meter (LP-3A, Beijing Material Science), and a source meter (Keysight 2902B) was used to measure the I-V properties. A mechanical platform (ESM303, Mark-10) was used to provide cyclic bending to flexible photodetectors.

Calculations on the projected shadow area of a deformed black PDMS pillar: According to the coordinate in Fig. 2e, we set *a* as the distance of the projection of the pillar highest point to point "*o*", and *b* as the distance of the projection of the leftmost point to point "*o*". θ is the angle between the top surface of the pillar and the horizontal direction, and *r* is the radius of the pillar. As shown in Fig. 2e, the projected area of a deformed black PDMS pillar can be regarded as the sum of three regions (i.e., S_1, S_2, and S_3). S_1 is the bottom surface area of the pillar, which can be expressed as πr^2, S_3 is the projected area by the top surface of the pillar, which can be expressed as $\pi r^2\cos\theta$. Notably, the sum of S_2', 1/2 S_1, and 1/2 S_3 can form a rectangle area, i.e., S_2', which can be expressed as $2r(a-r+r\cos\theta)$. Therefore, the projected shadow area of a deformed black PDMS pillar under a specific airflow speed can be expressed as,

$$S_{shadow} = \frac{1}{2}\pi r^2 - 2r^2 + \left(1-\frac{\pi}{4}\right)ra + \left(1+\frac{\pi}{4}\right)rb \quad (2)$$

where the values of "*a*" and "*b*" can be directly measured from the simulations or optical microscope images.

Fabrication of the hemispherical sensor array: PI sheet was utilized to fabricate the hemispherical substrate. As shown in Fig. S19, the three-dimensional hemispherical structure can be flattened into a two-dimensional pattern. Therefore, laser-cutting was utilized to define the required pattern of the PI sheet, consisting 12 equal parts. After that, attaching the patterned PI with a rigid and hemispherical polymethyl methacrylate (PMMA) mold by adhesive formed the hemispherical substrate. The location of the sensor array on the hemispherical substrate is critical. As shown in Fig. S19, a typical PI part is divided into three regions, which have the same height. For the situation that transferring the sensor onto Region I, the differences among the optoelectronic response obtained from each sensor of the sensing array are inconspicuous (similar to the planar array), making the following 3-axis airflow sensing difficult. If transferring the sensor onto Region III, the light incident angle is large, and the optoelectronic response degrades, as shown in Fig. 4i. Therefore, the sensor transferred on Region II, with the angle between the corresponding tangent line and the vertical direction being close to 45°, i.e., the middle for both horizontal and vertical lines, as highlighted in Fig. S19. During the experiment, the transfer of the sensor with good alignment to the target position was performed under a microscope.

Setup of deep neural network: To analyze the relationship between airflow angle and photocurrent variations of sensors, the incident angles (θ and φ) of the airflow were assumed to be two functions, named as *f* and *g*, of the photocurrent variations ($\frac{\Delta I}{I}_{sensor1}$, $\frac{\Delta I}{I}_{sensor2}$, $\frac{\Delta I}{I}_{sensor3}$, $\frac{\Delta I}{I}_{sensor4}$, $\frac{\Delta I}{I}_{sensor5}$, and $\frac{\Delta I}{I}_{sensor6}$), which can be written as,

$$\theta = f\left(\frac{\Delta I}{I_{sensor1}}, \frac{\Delta I}{I_{sensor2}}, \frac{\Delta I}{I_{sensor3}}, \frac{\Delta I}{I_{sensor4}}, \frac{\Delta I}{I_{sensor5}}, \frac{\Delta I}{I_{sensor6}}\right), \quad (3)$$

$$\varphi = g\left(\frac{\Delta I}{I_{sensor1}}, \frac{\Delta I}{I_{sensor2}}, \frac{\Delta I}{I_{sensor3}}, \frac{\Delta I}{I_{sensor4}}, \frac{\Delta I}{I_{sensor5}}, \frac{\Delta I}{I_{sensor6}}\right). \quad (4)$$

In the deep neural networks, the loss function and optimization algorithm are BCEWithLogitsLoss and adaptive moment estimation, respectively. A multichannel data set contains 73×6 photocurrent variations data in each channel, which is collected from traversing measurements of various structures and introduced into a 7-layer hidden layer. Because θ and φ are orthogonal in spherical coordinate system, the functions *f* and *g* are independent of each other.

CRediT authorship contribution statement

Ziyu Zhang: Methodology, Investigation, Formal analysis. **Miao Zhang:** Methodology, Investigation. **Xiaozhong Wu:** Writing – review & editing, Writing – original draft, Methodology, Investigation, Data curation. **Chengming Jiang:** Methodology, Investigation, Formal analysis. **Zhongying Xue:** Methodology, Investigation. **Yifei Zhang:** Methodology, Investigation. **Min Liu:** Methodology, Investigation, Funding acquisition. **Yanle He:** Methodology, Investigation. **Deyu Meng:** Methodology, Investigation. **Junjie Zhou:** Methodology, Investigation. **Qinglei Guo:** Writing – review & editing, Writing – original draft, Supervision, Investigation, Funding acquisition, Conceptualization. **Yang Wang:** Methodology, Investigation. **Yongfeng Mei:** Writing – review & editing, Writing – original draft, Supervision, Funding acquisition, Formal analysis, Conceptualization. **Haonan Zhao:** Methodology, Investigation, Formal analysis. **Zengfeng Di:** Writing – review & editing, Writing – original draft, Supervision, Funding acquisition, Formal analysis, Conceptualization.

Declaration of Competing Interest

The authors declare that they have no known competing financial interests or personal relationships that could have appeared to influence the work reported in this paper.

Acknowledgements

This work was supported by the STI 2030-Major Projects (Grant No. 2022ZD0209900), National Natural Science Foundation of China (Grant Nos. 51925208 and 62375054, and 523B2107), the Natural Science Foundation of Shandong Province in China (Grant No. ZR2021MF008), and the Open Research Fund of State Key Laboratory of Materials for Integrated Circuits (Grant No. SKLJC-K2024–02).

Appendix A. Supporting information

Supplementary data associated with this article can be found in the online version at doi:10.1016/j.nanoen.2025.110659.

Data availability

Data will be made available on request.

References

[1] C. Chen, J.L. Xu, Q. Wang, X.L. Li, F.Q. Xu, Y.C. Gao, Y.B. Zhu, H.A. Wu, J.W. Liu, Biomimetic multimodal receptors for comprehensive artificial human somatosensory system. Adv. Mater. 36 (2024) 2313228.
[2] D. Pan, J. Hu, B. Wang, X. Xia, Y. Cheng, C.H. Wang, Y. Lu, Biomimetic wearable sensors: emerging combination of intelligence and electronics. Adv. Sci. 11 (2023) 2303264.
[3] H.R. Schone, M. Udeozor, M. Moninghoff, B. Rispoli, J. Vandersea, B. Lock, L. Hargrove, T.R. Makin, C.I. Baker, Biomimetic versus arbitrary motor control strategies for bionic hand skill learning, Nat. Hum. Behav. 8 (2024) 1108.
[4] Y.L. Wang, J. Su, G.Y. Ouyang, S.Y.Y. Geng, M.C. Ren, W.L. Pan, J. Bian, M.H. Cao, Flexible Zn-TCPP nanosheet-based memristor for ultralow-power biomimetic sensing system and high-precision gesture recognition, Adv. Funct. Mater. 34 (2024) 2316397.
[5] S. Li, A. Liu, W. Qiu, Y. Wang, G. Liu, J. Liu, Y. Shi, Y. Li, J. Li, W. Cai, C. Park, M. Ye, W. Guo, An all-protein multisensory highly bionic skin. ACS Nano 18 (2024) 4579.
[6] X. Luo, C. Chen, Z. He, M. Wang, K. Pan, X. Dong, Z. Li, B. Liu, Z. Zhang, Y. Wu, C. Ban, R. Chen, D. Zhang, K. Wang, Q. Wang, J. Li, G. Lu, J. Liu, Z. Liu, W. Huang, A bionic self-driven retinomorphic eye with ionogel photosynaptic retina, Nat. Commun. 15 (2024) 3086.
[7] K. Liu, M. Wang, C. Huang, Y. Yuan, Y. Ning, L. Zhang, P. Wan, Flexible bioinspired healable antibacterial electronics for intelligent human-machine interaction sensing. Adv. Sci. 11 (2023) 2305672.
[8] H. Niu, H. Li, S. Gao, Y. Li, X. Wei, Y. Chen, W. Yue, W. Zhou, G. Shen, Perception-to-cognition tactile sensing based on artificial-intelligence-motivated human full-skin bionic electronic skin. Adv. Mater. 34 (2022) 2202622.
[9] P. Zhang, Z. Li, Y. Wang, W. Sun, K. Zhu, Q. Li, B. Li, Z. Wang, K. Wang, Z. Zheng, W. Liu, Electronic skin with biomimetic structures realizes excellent isothermal regulation, Nano Energy 121 (2024) 109189.
[10] Z. Liu, B. Tian, Y. Li, J. Lei, Z. Zhang, J. Liu, Q. Lin, C. Lee, Z. Jiang, A large-area bionic skin for high-temperature energy harvesting applications, Nano Res 16 (2023) 10245.
[11] X.C. Meng, C.C. Zhang, H.R. Xie, S.C. Niu, Z.W. Han, L.Q. Ren, A continuous pressure positioning sensor with flexible multilayer structures based on a combinatorial bionic strategy. Adv. Funct. Mater. 34 (2024) 2314479.
[12] X. Hong, Y. Zhao, C. Gong, J. Chao, B. Lv, Z. Xu, L. Xu, W. Zheng, Polyborosiloxane-encapsulated carbon nanotube/polyurethane foams for multifunctional pressure memory and pain bionic sensors. ACS Appl. Nano Mater. 6 (2023) 7543.
[13] J. Li, Z. Yao, X. Meng, X. Zhang, Z. Wang, J. Wang, G. Ma, L. Liu, J. Zhang, S. Niu, Z. Han, L. Ren, High-fidelity, low-hysteresis bionic flexible strain sensors for soft sachines. ACS Nano 18 (2024) 2520.
[14] K.Y. Dong, M. Wei, Q. Zhou, B.F. He, B.B. Gao, Bionic diffractive meta-silk patch for visually flexible wearables. Laser Photonics Rev. 18 (2024) 2300972.
[15] Y.P. Yang, L.L. Kong, B. Huang, B.F. Lin, L.H. Fu, C.H. Xu, A high-sensitive rubber-based sensor with integrated strain and humidity responses enabled by bionic gradient structure. Adv. Funct. Mater. (2024) 2400789.
[16] X. Wang, S. Yang, Z. Qin, B. Hu, L. Bu, G. Lu, Enhanced multiwavelength response of flexible synaptic transistors for human sunburned skin simulation and neuromorphic computation. Adv. Mater. 35 (2023) 2303699.
[17] Q.B. Zhu, B. Li, D.D. Yang, C. Liu, S. Feng, M.L. Chen, Y. Sun, Y.N. Tian, X. Su, X. M. Wang, S. Qiu, Q.W. Li, X.M. Li, H.B. Zeng, H.M. Cheng, D.M. Sun, A flexible ultrasensitive optoelectronic sensor array for neuromorphic vision systems, Nat. Commun. 12 (2021) 1798.
[18] Z. Gong, W. Di, Y. Jiang, Z. Dong, Z. Yang, H. Ye, H. Zhang, H. Liu, Z. Wei, Z. Tu, D. Li, J. Xiang, X. Ding, D. Zhang, H. Chen, Flexible calorimetric flow sensor with unprecedented sensitivity and directional resolution for multiple flight parameter detection, Nat. Commun. 15 (2024) 3091.
[19] S. Zhao, R. Zhu, Electronic skin with multifunction sensors based on thermosensation. Adv. Mater. 29 (2017) 3091.
[20] S. Chun, W. Son, C. Choi, H. Min, J. Kim, H.J. Lee, D. Kim, C. Kim, J.-s Koh, C. Pang, Bioinspired hairy skin electronics for detecting the direction and incident angle of airflow. ACS Appl. Mater. Interfaces 11 (2019) 13608.
[21] Z. Liu, D. Qi, W.R. Leow, J. Yu, M. Xiloyannnis, L. Cappello, Y. Liu, B. Zhu, Y. Jiang, G. Chen, L. Masia, B. Liedberg, X. Chen, 3D-Structured stretchable strain sensors for out-of-plane force detection, Adv. Mater. 30 (2018) 1707285.
[22] Z. Xu, K. Wu, S. Zhang, Y. Meng, H. Li, L. Li, Highly sensitive airflow sensors with an ultrathin reduced graphene oxide film inspired by gas exfoliation of graphite oxide, Mater. Horiz. 4 (2017) 383–388.
[23] L. Huang, Y. Liu, G. Li, Y. Song, J. Su, L. Cheng, W. Guo, G. Zhao, H. Shen, Z. Yan, B.Z. Tang, R. Ye, Ultrasensitive, fast-responsive, directional airflow sensing by bioinspired suspended graphene fibers. Nano Lett. 23 (2023) 597.
[24] Y. Bian, Y. Zhang, X. Xia, Design and fabrication of a multi-electrode metal-core piezoelectric fiber and its application as an airflow sensor. J. Bionic Eng. 13 (2016) 416.
[25] J. Wang, W. Ding, L. Pan, C. Wu, H. Yu, L. Yang, R. Liao, Z.L. Wang, Self-powered wind sensor system for detecting wind speed and direction based on a triboelectric nanogenerator. ACS Nano 12 (2018) 3954.
[26] L. Su, H. Wang, Z. Tian, H. Wang, Q. Cheng, W. Yu, Low detection limit and high sensitivity wind speed sensor based on triboelectrification-induced electroluminescence. Adv. Sci. 6 (2019) 1901980.
[27] Z. Wu, J. Ai, Z. Ma, X. Zhang, Z. Du, Z. Liu, D. Chen, B. Su, Flexible out-of-plane wind sensors with a self-powered feature inspired by fine hairs of the spider. ACS Appl. Mater. Interfaces 11 (2019) 44865.
[28] S. Huang, B. Zhang, Y. Lin, C.-S. Lee, X. Zhang, Compact biomimetic hair sensors based on single silicon nanowires for ultrafast and highly-sensitive airflow detection. Nano Lett. 21 (2021) 4684.
[29] J. Luo, N. Ji, W. Zhang, P. Ge, Y. Liu, J. Sun, J. Wang, Q. Zhuo, C. Qin, L. Dai, Ultrasensitive airflow sensor prepared by electrostatic flocking for sound recognition and motion monitoring, Mater. Horiz. 9 (2022) 1503.
[30] M. Hu, Y. Gao, Y. Jiang, H. Zeng, S. Zeng, M. Zhu, G. Xu, L. Sun, High-performance strain sensors based on bilayer carbon black/PDMS hybrids, Adv. Compos. Hybrid. Ma. 4 (2021) 514.

[31] S.M. Khare, A. Awasthi, V. Venkataraman, S.P. Koushika, Colored polydimethylsiloxane micropillar arrays for high throughput measurements of forces applied by genetic model organisms, Biomicrofluidics 9 (2015) 014111.
[32] H. Zhao, Z. Xue, X. Wu, Z. Wei, Q. Guo, M. Xu, C. Qu, C. You, Y. Mei, M. Zhang, Z. Di, Q. Guo, Biodegradable germanium electronics for integrated biosensing of physiological signals, npj Flex. Electron. 6 (2022) 63.
[33] P. Lin, Q. Guo, Complementary optoelectronic interaction of n^{+}-Si/p-Ge heterojunctions fabricated via transfer printing toward broadband photodetectors. Appl. Phys. Lett. 124 (2024) 162103.
[34] C.Y. You, B.F. Hu, B.R. Xu, Z.Y. Zhang, B.M. Wu, G.S. Huang, E.-M. Song, Y.-F. Mei, Foldable-circuit-enabled miniaturized multifunctional sensor for smart digital dust, Chip 1 (2022) 100034.
[35] Q. Guo, Z. Di, M.G. Lagally, Y. Mei, Strain engineering and mechanical assembly of silicon/germanium nanomembranes, Mat. Sci. Eng. R. 128 (2018) 1.
[36] G. Li, Z. Ma, C. You, G. Huang, E. Song, R. Pan, H. Zhu, J. Xin, B. Xu, T. Lee, Z. An, Z. Di, Y. Mei, Silicon nanomembrane phototransistor flipped with multifunctional sensors toward smart digital dust, Sci. Adv. 6 (2020) eaaz6511.
[37] D. Qi, K. Zhang, G. Tian, B. Jiang, Y. Huang, Stretchable electronics based on PDMS substrates. Adv. Mater. 33 (2020) 2003155.
[38] C. Qu, Q. Guo, X. Wu, C. You, B. Wu, Z. Zhang, Y. Mei, Matryoshka-inspired continuous assembly of flexible silicon microribbons and photodetectors via selective transfer printing, Mat. Today Phys. 35 (2023) 101090.
[39] Y. Zhang, R. Zhou, S. Ruan, Y. Ma, C. Liu, Y. Chen, J. Zhou, An efficient MSM UV photodetector with an ultra-low dark current enhanced by a back to back TiO2/PbTiO3 PN heterojunction, Appl. Phys. Lett. 123 (2023) 131105.
[40] K. Sim, S. Chen, Z. Li, Z. Rao, J. Liu, Y. Lu, S. Jang, F. Ershad, J. Chen, J. Xiao, C. Yu, Three-dimensional curvy electronics created using conformal additive stamp printing, Nat. Electron. 2 (2019) 471.
[41] C. Qu, Q. Guo, G. Huang, Y. Mei, Local cracking-induced scalable flexible silicon nanogaps for dynamically tunable surface enhanced Raman scattering substrates, Adv. Mater. Interfaces 8 (2021) 2100661..
[42] Y. Chen, Q. Guo, G. Huang, G. Li, L. Wang, Z. Tian, Y. Qin, Z. Di, Y. Mei, Multifunctional nanocracks in silicon nanomembranes by notch-assisted transfer printing, ACS Appl. Mater. Interfaces 10 (2018) 25644–25651.
[43] P. Wang, M. Wang, J. Zhu, Y. Wang, J. Gao, C. Gao, Q. Gao, Surface engineering via self-assembly on PEDOT: PSS fibers: Biomimetic fluff-like morphology and sensing application, Chem. Eng. J. 425 (2021) 131551.
[44] W. Zhou, P. Xiao, Y. Liang, Q. Wang, D. Liu, Q. Yang, J. Chen, Y. Nie, S.W. Kuo, T. Chen, Bionic adaptive thin-membranes sensory system based on microspring effect for high-sensitive airflow perception and noncontact manipulation. Adv. Funct. Mater. 31 (2021) 2105323.
[45] H. Wang, S. Li, Y. Wang, H. Wang, X. Shen, M. Zhang, H. Lu, M. He, Y. Zhang, Bioinspired fluffy fabric with in situ grown carbon nanotubes for ultrasensitive wearable airflow sensor. Adv. Mater. 32 (2020) 1908214.
[46] Q. Jiang, K. Leu, X. Gong, F. Wang, R. Li, K. Wang, P. Zhu, Y. Zhao, Y. Zang, R. Zhang, High-Performance Airflow sensors based on suspended ultralong carbon nanotube crossed networks. ACS Appl. Mater. Interfaces 16 (2024) 20949.
[47] A. Talbi, L. Gimeno, J.C. Gerbedoen, R. Viard, A. Soltani, V. Mortet, V. Preobrazhensky, A. Merlen, P. Pernod, A micro-scale hot wire anemometer based on low stress (Ni/W) multi-layers deposited on nano-crystalline diamond for air flow sensing, J. Micromech. Microeng. 25 (2015) 125029.
[48] Q. Jiang, R. Li, F. Wang, X. Shi, F. Chen, Y. Huang, B. Wang, W. Zhang, X. Wu, F. Wei, R. Zhang, Ultrasensitive airflow sensors based on suspended carbon nanotube networks. Adv. Mater. 34 (2022) 2107062.
[49] M.R. Maschmann, G.J. Ehlert, B.T. Dickinson, D.M. Phillips, C.W. Ray, G.W. Reich, J.W. Baur, Bioinspired carbon nanotube fuzzy fiber hair sensor for air-flow detection. Adv. Mater. 26 (2014) 3230.
[50] T. Ye, J. Chen, X. Tang, K. Li, Biomimetic hair-assisted GaN optical devices for bidirectional airflow detection, Microsyst. Nanoeng. 10 (2024) 166.
[51] E. Fujiwara, T. Delfino, T. Cabral, C.M. Cordeiro, All-optical fiber anemometer based on the pitot-static tube, IEEE Trans. Instrum. Meas. 69 (2020) 1805–1811.
[52] P. Wang, Y. Zhao, Y. Yang, D. Bi, Research on a novel variable-area optical fiber gas flow sensor, Sens. Actuator A: Phys. 221 (2015) 29–32.
[53] J. Liu, S. Jiang, W. Xiong, C. Zhu, K. Li, Y. Huang, Self-healing kirigami assembly strategy for conformal electronics. Adv. Funct. Mater. 32 (2022) 2109214.
[54] S. Liu, J. He, Y. Rao, Z. Dai, H. Ye, J.C. Tanir, Y. Li, N. Lu, Conformability of flexible sheets on spherical surfaces, Sci. Adv. 9 (2023) eadf2709.
[55] W. Lee, Y. Liu, Y. Lee, B.K. Sharma, S.M. Shinde, S.D. Kim, K. Nan, Z. Yan, M. Han, Y. Huang, Y. Zhang, J.-H. Ahn, J.A. Rogers, Two-dimensional materials in functional three-dimensional architectures with applications in photodetection and imaging, Nat. Commun. 9 (2018) 1417.
[56] Z. Zhang, B. Wu, Y. Wang, T. Cai, M. Ma, C. You, C. Liu, G. Jiang, Y. Hu, X. Li, X.-Z. Chen, E. Song, J. Cui, G. Huang, S. Kiravittaya, Y. Mei, Multilevel design and construction in nanomembrane rolling for three-dimensional angle-sensitive photodetection, Nat. Commun. 15 (2024) 3066.

Xiaozhong Wu received his B.S. degree from Changchun University of Science and Technology. Now, he is a Ph.D. student at the School of Integrated Circuits of Shandong University. His current research interest focuses on flexible multi-functional photodetectors and their applications.

Ziyu Zhang received his B.S. degree in Material Physics from Fudan University. He is pursuing his Ph.D. degree in Material Physics and Chemistry in Fudan University. His current research interest focusses on the design, fabrication, and application of three-dimensional rolled-up nanomembrane structures for advanced optoelectronics.

Haonan Zhao received the Ph.D. degree from the School of Integrated Circuits, Shandong University, Jinan, China, in 2023. She currently is a postdoc with the School of Integrated Circuits, Shandong University, Jinan, China. Her research interest main focuses on flexible/ degradable electronics, near-field wireless energy transfer and electrical nerve stimulation.

Yang Wang received his B.S. degree in Materials Physics and his Ph. D. in Materials Science and Technology from Fudan University, China. He is currently a postdoctoral researcher at Fudan University, focusing on rolled-up nanomembrane devices and their applications, including microrobots, silicon-based optics and optoelectronics.

Junjie Zhou graduated from Yantai University with a Bachelor's degree in Engineering. He is currently studying at the School of Integrated Circuits, Shandong University as a doctoral candidate. His current research focuses on biodegradable transient electronic devices.

Deyu Meng received his BSc degree at Chongqing Normal University. Now, he is a Ph.D. student at the School of Integrated Circuits of Shandong University. His research interests include Flexible multi-functional sensors and Wearable electronics.

Yanle He received his bachelor's degree from Shandong University in 2022. Currently, he studies as a Ph.D. student group in School of integrated Circuits, Shandong University. His research focuses on manufacture and application of silicon-based flexible optoelectronic devices for biomedical applications.

Min Liu received her B.S. degree from Shandong University and Ph.D. degree from Peking University. She worked in the National University of Singapore as a post-doctor for optical physics. She joined the School of Integrated Circuits, Shandong University as an associated professor. Her research interest focuses on the photoelectric device, nonlinear optics of multi-functional materials.

Yifei Zhang received his B.S. and M.S. degrees in Electrical Engineering at the Beijing Institute of Technology in 2006 and 2009, respectively, and his Ph.D. degree in the Department of Electrical and Computer Engineering, University of Delaware in 2016. He is currently a Qilu Professor in the School of Integrated Circuits, Shandong University, Shandong, China, where he established the TeraMillie Laboratory for the circuits and devices at terahertz and millimeter wave frequencies. He has authored and coauthored more than 60 international papers and held more than 10 patents.

Zhongying Xue received his Ph.D. degree from Chinese Academy of Sciences. He joined the Shanghai Institute of Microsystem and Information Technology, Chinese Academy of Sciences as a researcher. His research interest focuses on the preparation and mechanism of large size silicon wafer, SOI wafer and graphene.

Chengming Jiang received his Ph.D. in Material Science in the University of Alabama, USA. Currently, he works as an associate professor in the Department of Mechanical Engineering at the Dalian University of Technology, China. His research includes one dimensional nanomaterial in optical device, OLED, and photon actions in organic-inorganic semiconducting materials.

Miao Zhang received the Ph.D. degree from the Shanghai Institute of Microsystem and Information Technology (SIMIT), Chinese Academy of Sciences (CAS), Shanghai, China, in 1998. She is a Professor with the Shanghai Institute of Microsystem and Information Technology, CAS. Her current research interests include high mobility semiconductors, silicon-on-insulator materials, etc.

Zengfeng Di received his B.S. degree from Nanjing University and Ph.D. degree from Shanghai Institute of Microsystems and Information Technology, Chinese Academy of Sciences. He joined the Shanghai Institute of Microsystems and Information Technology, Chinese Academy of Sciences as a professor in 2010. His research interests are SOI materials, devices and circuits, low-dimensional materials and devices, and integrated circuit design.

Yongfeng Mei received his B.S. and M.S. degree from Nanjing University, and Ph.D. degree from City University of Hong Kong. Following post-doctoral/staff scientist at Max Planck Institute for Solid State Research, as well as group leader/staff scientist at Leibniz Institute for Solid State and Materials Research Dresden, he joined Department of Materials Science of Fudan University as a professor in materials physics. His research interest focuses on the development of nanomembranes and their properties in optics, optoelectronics, flexible electronics, and micro/nanoscale robotics.

Qinglei Guo received his Ph.D. degree from Shanghai Institute of Microsystems and Information Technology, Chinese Academy of Sciences. He joined the School of Integrated Circuits, Shandong University as a professor in 2018. His research interest focuses on inorganic semiconductor-based flexible/transient electronics, wide band-gap semiconductor devices and integration.